Published in final edited form as:
Chem Erde. 2019 December ; 79(4): . doi:10.1016/j.chemer.2019.125543.

Origin of ^{16}O-rich fine-grained Ca-Al-rich inclusions of different mineralogy and texture

Jangmi Han[a,b,c,*], **Benjamin Jacobsen**[d], **Ming-Chang Liu**[e], **Adrian J. Brearley**[a], **Jennifer E. Matzel**[d], **Lindsay P. Keller**[c]

[a]Department of Earth and Planetary Sciences, MSC03-2040, University of New Mexico, Albuquerque, NM 87131, USA

[b]Lunar and Planetary Institute, USRA, 3600 Bay Area Boulevard, Houston, TX 77058, USA

[c]ARES, NASA Johnson Space Center, 2101 NASA Parkway, Houston, TX 77058, USA

[d]Nuclear and Chemical Sciences Division, Lawrence Livermore National Laboratory, Livermore, CA 94550, USA

[e]Department of Earth, Planetary, and Space Sciences, University of California, Los Angeles, Los Angeles, CA 90095, USA

Abstract

A coordinated mineralogical and oxygen isotopic study of four fine-grained calcium-, aluminum-rich inclusions (CAIs) from the ALHA77307 CO3.0 carbonaceous chondrite was conducted. Three of the inclusions studied, 05, 1–65, and 2–119, all have nodular structures that represent three major groups, melilite-rich, spinel-rich, and hibonite-rich, based on their primary core mineral assemblages. A condensation origin was inferred for these CAIs. However, the difference in their primary core mineralogy reflects unique nebular environments in which multiple gas-solid reactions occurred under disequilibrium conditions to form hibonite, spinel, and melilite with minor perovskite and Al,Ti-rich diopside. A common occurrence of a diopside rim on the CAIs records a widespread event that marks the end of their condensation as a result of isolation from a nebular gas. An exception is a rare inclusion 2–112 that contains euhedral spinel crystals embedded in melilite, suggesting this CAI had been re-melted. All of the fine-grained CAIs analyzed in ALHA77307 are uniformly ^{16}O-rich with an average Δ^{17}O value of ~−22 ± 5‰ (2σ), indicating no apparent correlation between their textures and oxygen isotopic compositions. We therefore conclude that a prevalent ^{16}O-rich gas reservoir existed in a region of the solar nebula where CO3 fine-grained CAIs formed, initially by condensation and then later, some of them were reprocessed by melting event(s).

Keywords

calcium-aluminum-rich inclusions; microstructures; oxygen isotopes; solar nebula

[*]corresponding author. han@lpi.usra.edu.

1. INTRODUCTION

Calcium-, aluminum-rich inclusions (CAIs) are the oldest objects known to have formed within the early solar nebula (e.g., Connelly et al., 2012). They are composed of refractory minerals that are predicted to be among the first to condense from a gas of solar composition (Ebel, 2006). However, CAIs show significant variations in textures, mineralogy, and chemical and isotopic compositions within and among different chondrite groups, indicating complex formation histories under various physicochemical conditions (MacPherson, 2014). Possible formation processes for CAIs include gas-solid condensation, melting, evaporation, and/or shock that occurred in the solar nebula (MacPherson, 2014). In general, many coarse-grained CAIs found in CV3 chondrites are thought to have once been partially or completely re-melted (e.g., MacPherson and Grossman, 1981; Simon et al., 1999), whereas fine-grained CAIs commonly found in CO, CR, CM, and CV chondrites represent the products of high-temperature condensation that experienced minimal melting (e.g., Krot et al., 2004a; Han and Brearley, 2017). The texture, mineralogy, and chemical and isotopic compositions of CAIs are therefore a valuable resource for understanding the primordial conditions of the earliest dust-forming environments in the solar nebula, in particular the reservoirs they formed.

The oxygen isotopic compositions of CAIs are distributed along the carbonaceous chondrite anhydrous mineral (CCAM) line on a three-isotope plot over a range between oxygen isotopic compositions of protosolar ($\delta^{18,17}O \approx -50‰$ to $-60‰$) and planetary ($\delta^{18,17}O \approx$ ~0‰) reservoirs (e.g., Clayton et al., 1977; Young and Russell, 1998; Ushikubo et al., 2012). A large degree of oxygen isotopic heterogeneity is often observed within individual CAIs and their rims from CV3 chondrites. Simon et al. (2011) showed that a coarse-grained Type A CAI A37 from the Allende CV3 chondrite exhibits $^{17,18}O$-enrichments toward its margin, approaching a planetary-like isotopic composition, then an extreme shift to protosolar-like ^{16}O-rich compositions through a surrounding rim. This heterogeneous oxygen isotope distribution may be related to primary high-temperature nebular processes involving gas reservoirs with various oxygen isotopic compositions, implying transport of CAIs between distinct reservoirs in the solar nebula or evolution of the gas composition near the protosun (e.g., Yurimoto et al., 1998; Park et al., 2012; Simon et al., 2016; Kawasaki et al., 2017). Numerical models of solar nebular evolution suggest that CAIs could experience extremely complex transport paths through the protoplanetary disk, interacting with multiple gas reservoirs that have a wide range of nebular density, pressure, and temperature conditions (e.g., Ciesla, 2010; Boss et al., 2012). However, oxygen isotopic records in CAIs, in particular from CV3 chondrites, are often complicated by secondary low-temperature parent body processes involving ^{16}O-poor fluids (e.g., Wasson et al., 2001; Itoh et al., 2004; Bodénan et al., 2014; Krot et al., 2017, 2019). Wasson et al. (2001) found that fine-grained CAI melilite in the Kainsaz CO3.2 and Ornans CO3.3 chondrites shows significant, but various degrees of $^{17,18}O$-enrichments relative to that in the Colony CO3.0 chondrite, suggesting that oxygen isotopic compositions of melilite can be easily disturbed by very low-grade parent body alteration without any textural or compositional modification.

Here we report the mineralogy, petrology, and oxygen isotopic compositions of four fine-grained CAIs in the Allan Hills (ALH) A77307 CO3.0 carbonaceous chondrite for the

following important reasons: (1) this meteorite is one of the least-altered CO chondrites (e.g., Grossman and Brearley, 2005), thus providing important clues into the primary nebular characteristics of CAIs; and (2) fine-grained CAIs in carbonaceous chondrites are generally regarded as aggregates of high-temperature nebular condensates that experienced no or little melting (e.g., Krot et al., 2004a; Han and Brearley, 2017). Our study elucidates the connection between the mineralogy, textures, and oxygen isotopic compositions of fine-grained CAIs in ALHA77307 and the variations in oxygen isotopic compositions across their interiors and rims. The implications for the formation processes and conditions of these CAIs are considered.

2. METHODS

Four fine-grained CAIs (05, 1–65, 2–119, and 2–112) in two petrographic thin sections of ALHA77307 (ALH 77307,40 and, 76) were studied using a FEI Quanta 3D field emission gun scanning electron microscope (SEM)/focused ion beam (FIB) instrument fitted with an EDAX Apollo 40 SDD Energy Dispersive Spectroscopy system at the University of New Mexico (UNM). The instrument was operated at 30 kV accelerating voltage in the high-vacuum mode, using beam currents of 2–23 nA for backscattered electron (BSE) imaging and 23 nA for x-ray mapping. Quantitative wavelength-dispersive spectroscopy analyses of individual minerals in the ALHA77307 CAIs were collected with a JEOL JXA-8200 electron microprobe at UNM. All analyses were obtained at 15 kV accelerating voltage, 20 nA beam current, and 1 μm spot size. Elemental calibration was carried out using CM Taylor Company Microprobe Standards as follows: Mg, Si, and Fe on olivine, Al and K on orthoclase, Ca on diopside, Mn on spessartine, Cr on chromite, Na on albite, V on V-metal, and Ti on rutile. Data were reduced using the modified ZAF correction procedure and reported in Table 1.

Oxygen isotopic compositions of the ALHA77307 CAIs were measured *in situ* using a CAMECA NanoSIMS 50 at the Lawrence Livermore National Laboratory and a CAMECA ims-1290 ion microprobe at UCLA. The NanoSIMS protocol for measuring oxygen isotopes is described in Simon et al. (2011). A ~10 pA Cs^+ primary beam with a diameter of ~200 nm was rastered over 2×2 μm^2 areas. Negative secondary ions were acquired by simultaneously measuring $^{16}O^-$ on a Faraday cup (FC) and $^{17}O^-$, $^{18}O^-$, and $^{28}Si^-$ on electron multipliers. A mass resolving power of ~7000 was used to minimize the contribution from $^{16}OH^-$ to $^{17}O^-$. Instrumental mass fractionation was determined by measuring matrix matched terrestrial standards (Burma spinel, San Carlos olivine, and San Carlos pyroxene). The external reproducibility of our standards on $\Delta^{17}O$ was <6‰ (2σ).

Oxygen isotope analysis on the UCLA ims-1290 ion microprobe was carried out in multi-collection mode with 3 FCs. A 3.5 nA, 20 keV Cs^+ primary beam with a diameter of ~20 μm was used. Secondary $^{16}O^-$ and $^{18}O^-$ ions were collected on off-axis L'2 (10^{10} Ω) and H1 (10^{11} Ω), respectively, at mass resolution of ~2,500, whereas the $^{17}O^-$ signal was measured with the axial FC2 FC (10^{11} Ω) at mass resolution of ~7,000. Instrumental mass fractionation was characterized by using a suite of terrestrial standards (Burma spinel, San Carlos olivine, and San Carlos pyroxene). The external reproducibility of $\Delta^{17}O$ on standards is ~1‰ (2σ).

It should be noted that no corrections for matrix effects were performed for hibonite, perovskite, melilite due to the lack of proper standards for those minerals. However, these did not affect the determination of $\Delta^{17}O$ values for hibonite, perovskite, and melilite. Therefore, oxygen isotope data obtained both from the NanoSIMS and the ims-1290 ion microprobe are reported in Table 2 only as deviations from the terrestrial mass fractionation line that are calculated as $\Delta^{17}O\ (‰) = \delta^{17}O - 0.52 \times \delta^{18}O$.

Following oxygen isotope measurements, two FIB sections were prepared from CAIs 1–65 and 2–119 using a FEI Quanta 3D 600 dual beam FIB-SEM at NASA Johnson Space Center (JSC). Targeted regions for the sections covered all different mineral phases observed in the inclusions. The FIB sections were characterized in detail using bright-field (BF) and dark-field (DF) images, high-resolution (HR) images, and selected area electron diffraction (SAED), using a JEOL 2500SE 200 kV field-emission scanning transmission electron microscope (STEM) at NASA JSC. In addition, chemical microanalyses and elemental mapping were carried out using a Thermo-Noran thin-window energy dispersive X-ray (EDX) spectrometer. Elemental X-ray maps were obtained using STEM raster mode with a scanned probe size of 2 nm and a dwell time of 50 μs/pixel. Successive rasters were added until <1% counting statistical errors were achieved for major elements. Data reduction was performed using the Cliff-Lorimer thin film approximation with experimental and theoretical K-factors determined from natural and synthetic standards.

3. RESULTS

A total of 319 fine-grained CAIs were identified from the two thin sections of ALHA77307; they are typically less than 200 μm in size and irregularly-shaped. Based on the observed primary core mineral assemblages, ALHA77307 CAIs can be divided into three major types: melilite-rich, spinel-rich, and hibonite-rich inclusions (Russell et al., 1998; Han and Brearley, 2017). The frequencies for each type are approximately 28%, 55%, and 17% of total found, respectively. In these CAIs, perovskite is a common accessory phase, but anorthite is completely absent. Most CAIs are rimmed by a single layer of diopside; olivine rims are very rare. Representative SEM and TEM images of the ALHA77307 CAIs analyzed in this study are presented in Figures 1–10, and average compositions of their individual mineral phases obtained using electron microprobe are listed in Table 1.

3.1. Melilite-Rich CAI 05

A detailed TEM study of CAI 05 was presented in Han and Brearley (2017); only a short summary of mineralogical and petrologic characteristics of this inclusion is provided below.

CAI 05 is a melilite-rich inclusion (Fig. 1), a common type of CAI in ALHA77307 and other CO3 chondrites (Russell et al., 1998; Simon and Grossman, 2015; Han and Brearley, 2017). This inclusion is a rounded object, 110 μm in diameter, with a distinct zoned structure (Figs. 1a, b). The CAI consists of a compact melilite-rich core completely enclosed by a 20–25 μm-thick porous mantle, followed by a discontinuous, 2 μm-thick rim of diopside. The melilite-rich core, 70 μm in diameter, is dominated by very gehlenitic melilite ($Åk_{\sim 5–10}$; Table 1) with fine-grained perovskite and spinel. The porous mantle consists of complex intergrowths of spinel and melilite with fine-grained perovskite (Figs. 1c, d). Spinel in the

mantle is more abundant than in the core and occurs either as very fine grains embedded in melilite or in a band that is concentrated in the outer region of the mantle. Subrounded to elongated perovskite grains <3 μm in size are randomly distributed throughout the inclusion.

Based on the TEM results presented in Han and Brearley (2017), the core consists of a dense aggregate of very gehlenitic melilite grains ($Åk_{\leq 2}$) having straight or slightly curved grain boundaries, but its edge is embayed by spinel and minor Al,Ti-rich diopside. Such very åkermanite-poor compositions were obtained from the outermost core and represent a narrower and lower range than EMPA data obtained from the inclusion center (Table 1). The mantle contains perovskite grains corroded by Al,Ti-rich diopside and minor spinel, finally embedded in melilite (Fig. 2a). All phases in the mantle share highly irregular grain boundaries with each other. Melilite in the mantle is gehlenitic with a range of $Åk_{1–17}$, but shows no systematic compositional zonation. Al,Ti-rich diopside is usually less than 1 μm thick, identified only by TEM, and shows relatively constant ranges of Al_2O_3 (24–26 wt%) and TiO_2 (8–14 wt%) throughout the mantle (Fig. 2b). Numerous pores are homogeneously distributed throughout the mantle and are dominantly present in melilite.

3.2. Spinel-Rich CAI 1–65

CAI 1–65 is a spinel-pyroxene inclusion with a size of 190×230 μm (Fig. 3). This CAI is a mineralogically-zoned inclusion consisting of subrounded to elongated nodules of spinel cores (<200 μm in size) corroded by thin layers of Al,Ti-rich diopside and minor melilite, finally surrounded by a 5–30 μm-thick diopside rim. In addition, minor forsteritic olivine is intergrown and shares convoluted grain boundaries with diopside in the outermost rim (Figs. 3c, d). Spinel is nearly pure $MgAl_2O_4$ with 0.15–0.32 wt% FeO, and diopside contains a range of Al_2O_3 (3.8–6.7 wt%) with very low TiO_2 (0.08–0.22 wt%) (Table 1).

The FIB section reveals the zonal sequence (Fig. 4): from the spinel core > intergrowth of spinel, Al,Ti-rich diopside, and minor melilite > Al-rich diopside with minor spinel and Al,Ti-rich diopside > forsterite > diopside > forsterite > finally to diopside. The grain size tends to decrease from the spinel core to the outermost diopside rim. The core consists of a compact aggregate of spinel grains (2.5–10 μm in size) with minor Al,Ti-rich diopside and perovskite having straight to curved grain boundaries and is highly embayed by complexly intergrown spinel and Al,Ti-rich diopside (Fig. 4a). Minor, subrounded melilite grains (<1 μm in size) also occur in this intergrowth layer and are partially to completely surrounded by spinel. All grains within the intergrowth layer have highly curved, unequilibrated grain boundaries (Fig. 5a). In contrast, the following outer layers from Al-rich diopside to diopside develop a higher degree of equilibrated grain boundaries between phases, often with straight grain boundaries and 120° triple junctions (Fig. 5b). In particular, forsterite grains display a columnar morphology, with a common elongation direction along their (001) and (011) planes for some grains. In these layers, the grain size ranges up to 5 μm, but mostly less than 3 μm.

Our TEM EDX analyses reveal a high degree of compositional variation in pyroxene that occurs over a distance of ~15 μm from the spinel core, between and within grains. The Al_2O_3 and TiO_2 contents in pyroxene vary up to 25 wt% and 19 wt%, respectively. In general, pyroxene becomes less Al,Ti-rich with increasing distance from the spinel core and

then finally pure diopside (≤1 wt% Al_2O_3) in contact with two olivine layers. However, the highest Al and Ti contents in pyroxene do not occur at the interfaces with the spinel core, but as patches in the intergrowth layer (Figs. 4b–e). Spinel is nearly $MgAl_2O_4$ with <0.5 wt% FeO. Spinel only in the core contains detectable TiO_2 (0.2–0.4 wt%) and V_2O_3 (0.2–0.3 wt %) in contrast to that in the intergrowth layer. Olivine is forsteritic with no detectable Fe content.

3.3. Hibonite-Rich CAI 2–119

CAI 2–119 is a hibonite-spinel inclusion with a size of 55×45 μm (Fig. 6). This CAI appears to have three nodules separated by a layer of Fe,S-rich phases, probably terrestrial weathering products, followed by a 0.5–10 μm-thick rim of diopside. The individual nodules consist of hibonite laths (7–25 μm in length and 1.5–8 μm in width) partially to completely surrounded by spinel. Perovskite grains up to 2 μm in size are present only in spinel (Fig. 6c). Hibonite contains 1.4–3.9 wt% TiO_2 and 0.93–2.4 wt% MgO. Spinel is nearly pure $MgAl_2O_4$ with ~0.8 wt% FeO (Table 1).

The FIB section contains a single hibonite crystal completely embedded in spinel grains with minor perovskite and Al,Ti-rich diopside (Figs. 7a, b). Hibonite is elongated normal to the *c** axis. No stacking faults was observed in hibonite. Spinel grains share embayed grain boundaries with adjacent hibonite and appear to have a platy morphology with their elongation direction normal to the *c** axis of hibonite (Figs. 7c, d). Al,Ti-rich diopside is identified only by TEM and appears to occur interstitially between spinel and mostly elongated (up to 300 nm thick and 1 μm long) along with surrounding spinel grains (Fig. 7c). Importantly, hibonite is in a crystallographic continuity only with spinel; there are no crystallographic orientation relationships between hibonite and Al,Ti-rich diopside. Analysis of diffraction patterns obtained from three different sets of the interfaces between hibonite and adjacent spinel grains, as well as the FFT patterns obtained from their HR-TEM images, yields the same crystallographic orientation relationships between them such that $[110]_{hibonite}//[011]_{spinel}$ and $(001)_{hibonite}//(111)_{spinel}$ (Fig. 8). The diopside rim consists of a compact aggregate of grains less than 2 μm in size having nearly equilibrium grain boundary microstructures, i.e., straight grain boundaries and 120° triple junctions (Figs. 9a, d).

Our TEM EDX analyses show that hibonite contains 1.5–2.1 wt% TiO_2 and 0.3–0.7 wt% MgO with no detectable zoning. Spinel is nearly $MgAl_2O_4$ with ≤0.1 wt% FeO. Pyroxene interstitial to spinel appears consistently Al,Ti-rich. However, its Al_2O_3 and TiO_2 contents could not be determined accurately due to inclined grain boundaries of Al,Ti-rich diopside shared with hibonite and spinel in the FIB section. In contrast, the rim pyroxene exhibits compositional variations within and between grains, with an overall range of ≤13 wt% Al_2O_3 and ≤4.5 wt% TiO_2. Figure 9 shows heterogeneous distributions of Al and Ti contents in pyroxene grains, revealing a complex intergrowth of zoned and unzoned diopside grains. Some grains are Al,Ti-poor, pure diopside constantly throughout the grains, but others are zoned, showing a progressive decrease in Al and Ti contents outward over a distance less than 1 μm.

3.4. Melilite-Rich CAI 2–112

CAI 2–112 is a melilite-rich inclusion 135×70 μm in size (Fig. 10). In the thin section, this CAI appears as two inclusions separated by fine-grained matrix, which may be fragments of a larger single inclusion, due to their close proximity and textural similarities. This CAI is a rare inclusion that shows a poikilitic texture with euhedral to subhedral spinel grains (1.5–8 μm in size) enclosed in melilite, rather than the layered structures that are common in other ALHA77307 CAIs, as described above. No diopside rim is observed. Melilite is gehlenitic ($Åk_{\sim 5–15}$) and appears zoned; our electron microprobe data show its åkermanite contents decrease gradually over a distance of ~ 100 μm from one end of the crystals to another (Fig. 10c). Spinel is nearly pure $MgAl_2O_4$ with 0.15–0.48 wt% FeO (Table 1).

3.5. Oxygen Isotopic Compositions

Oxygen isotopic compositions of minerals in the four ALHA77307 CAIs are listed in Table 2 and shown in Figure 11. Based on our NanoSIMS measurements, all the CAIs contain phases that are uniformly ^{16}O-rich with an average $\Delta^{17}O$ value of ~−22±5‰, regardless of the significant difference in their primary mineralogy and texture. The following ims-1290 analysis of CAI 2–112 melilite yielded $\Delta^{17}O = −26.8±0.5‰$, in a good agreement with the average $\Delta^{17}O$ value of −22.6±5.0‰ that were derived from the NanoSIMS measurements within errors. No systematic differences in oxygen isotopic compositions are observed between individual CAIs or between different minerals within the CAIs. The observed homogeneous oxygen isotopic compositions are similar to those previously reported from CAIs in the same meteorite ALHA77307 (Bodénan et al., 2014; Needham et al., 2017), as well as other pristine CO3.0 chondrites such as Colony, Yamato 81020, and Dominion Range 08006 (Wasson et al., 2001; Itoh et al., 2004; Ushikubo et al., 2017; Simon et al. 2019 a, b). Moreover, very similar oxygen isotopic compositions ($\Delta^{17}O \leq$~−20‰) were also reported from the least-altered, fine-grained CAIs in CM, CR, CH, and Acfer 094 chondrites (Aléon et al., 2002; Matzel et al., 2013; Krot et al., 2017; Ushikubo et al., 2017) and, in particular, from spinel and pyroxene in fine-grained CAIs from CV3 chondrites (Fagan et al., 2004; Aléon et al., 2005), which are highly resistant to subsequent oxygen isotopic exchange in the parent body setting (Ryerson and McKeegan, 1994).

4. DISCUSSION

4.1. CAIs 05, 1–65, and 2–119: High-temperature Condensates

The textural and mineralogical differences between the core and the mantle in melilite-rich CAI 05 (Fig. 1) suggest different formation processes or conditions for these two different zones. The core shows compact and equilibrated textures and has relatively narrow range of melilite compositions ($Åk_{\leq 10}$), suggesting its formation under conditions very close to equilibrium. We therefore infer that, after condensation of minor perovskite and spinel, condensation of gehlenitic melilite occurred to form the core. In contrast, the nearly rounded shape of this CAI (Figs. 1a, b) may indicate that its porous mantle is a zone that was processed by partial melting and evaporation after the formation of the compact core. As discussed in detail by Han and Brearley (2017), a melting origin for the mantle seems highly unlikely for several reasons: (1) all phases share highly curved grain boundaries with each other (Fig. 2a); (2) abundant pores are present and concentrated in the mantle (Figs. 1c, d);

(3) its bulk composition (in wt%: 17.34 SiO_2 + 5.89 TiO_2 + 38.88 Al_2O_3 + 8.50 MgO + 29.40 CaO) lies very close to that predicted for equilibrium condensates from a solar gas with no evident MgO and SiO_2 deficiencies (Grossman et al., 2000), indicating no or minimal modification of the mantle composition by evaporation that could have occurred during melting; (4) the crystallization sequence and path of a melt of its bulk composition inferred from the Stolper (1982) phase relations (spinel > melilite > anorthite > pyroxene, no perovskite expected) are not consistent with the observed textural relationships between phases (perovskite > spinel > melilite > pyroxene, no anorthite observed); and (5) the Stolper (1982) phase relations also expect melilite crystallized from a melt of its bulk composition to be strongly zoned with a starting composition $Åk_{>20}$, which is inconsistent with the observed composition range of unzoned melilite ($Åk_{1–17}$) in the mantle. Therefore, we conclude that the mantle of CAI 05 formed by a later stage of condensation onto the core of the initial inclusion. Dynamic and rapidly changing conditions (e.g., Ciesla, 2010; Boss et al., 2012) may have disturbed the condensation path of a gas reservoir, enabling perovskite, spinel, and melilite to resume condensation after the core formation by equilibrium condensation of melilite with minor perovskite and spinel. Melilite was a late phase that condensed interstitially to early-formed phases such as perovskite and spinel in the mantle, but did not entirely fill the void spaces, forming a porous aggregate. The observed compositional variation in melilite ($Åk_{1–17}$) may indicate that it condensed over a temperature range in a gas of constant composition (Han and Brearley, 2017); that is, melilite begun to condense as nearly pure gehlenite, but underwent reactions with gaseous Mg to form more åkermanitic melilite, as temperature fell (Yoneda and Grossman, 1995). Later, minor Al,Ti-rich diopside formed by a small degree of a reaction involving perovskite with minor spinel and melilite in the mantle. Finally, a thin layer of diopside formed on the mantle by a reaction of melilite with gaseous Mg and SiO (Yoneda and Grossman, 1995).

The spinel-rich CAI 1–65 (Fig. 3) shares many textural and mineralogical characteristics with those in CM, CV, and CR chondrites (MacPherson et al., 1983; Aléon et al., 2002; Krot et al., 2004a), but is smaller and has no evidence for secondary parent body alteration processes. The nebular processes that affected such spinel-cored, pyroxene-rimmed inclusions in carbonaceous chondrites appear to be very similar and widespread. Therefore, this inclusion can be interpreted as a primary condensation product that experienced no or a low degree of partial melting. We propose that distinct textures, mineral assemblages, and mineral chemistry through the zonal sequence observed in CAI 1–65 reflect a complex nebular history that involved an initial stage of the core formation by condensation under conditions close to equilibrium, followed by a dynamic stage of reactions of refractory solids in the cores with a nebular gas that produced complex fine-grained intergrowths in the rim. A similar two-stage formation history was also inferred based on TEM analyses of similar spinel-rich CAI-like objects in an amoeboid olivine aggregate from ALHA77307 (Han and Brearely, 2016). Our TEM observations of CAI 1–65 show a high degree of textural and compositional disequilibrium of the complex intergrowth layer of highly irregular Al,Ti-rich diopside, spinel, and melilite and its corroded appearance at the interface with the spinel core (Fig. 4). This intergrowth layer is best explained as a reaction zone in which spinel and melilite at the periphery of the cores reacted with a nebular gas to form Al,Ti-rich diopside (Han and Brearley, 2016). Because early-condensed Ti-rich solid phases are completely

absent, the gas was probably saturated with Ti, as well as Mg, and Si, and resulted in partial replacement of melilite and spinel by Al,Ti-rich diopside under conditions far from equilibrium (Krot et al., 2004b). Spinel in the cores, the earliest-formed primary condensation phase, was consumed as the main solid phase in the reaction with the nebular gas. The occurrence of minor melilite surrounded by spinel suggests that melilite may have reacted extensively with spinel and the nebular gas to supply Ca during diopside formation. Alternatively, only a small amount of melilite condensed during the core formation and therefore played only a minor role in the evolution of the CAI. As the reaction proceeded, the Ti in the gas phase was incorporated rapidly into diopside so that the condensing diopside composition evolved outward from Al,Ti-rich, through Al-rich, to Al,Ti-poor. A small amount of forsterite condensed directly from a nebular gas onto diopside (Krot et al., 2004b), followed by condensation of diopside, forsterite, and finally diopside. Thermodynamic equilibrium condensation models predict that forsterite begins to condense ~5–15 K lower than diopside (Ebel, 2006). Such oscillating condensation of diopside and forsterite on the inclusion exterior implies a rapid fluctuation in a narrow range of temperatures of a gas reservoir where these two phases were condensing alternatively, as the final stage in the formation sequence for CAI 1–65. In addition, the columnar morphology of forsterite grains is consistent with their nucleation and growth from a gas phase (Kobatake et al., 2008; Nozawa et al., 2009). Similar morphology were also observed from forsteritic olivine grains in the final layer of a Wark-Lovering rim (Keller et al. 2013).

The irregular shape and layered structure of hibonite-rich CAI 2–119 (Fig. 6) and the absence of detectable compositional zoning in hibonite (Fig. 7b) clearly indicate a condensation origin with hibonite as the first condensate, followed by perovskite, spinel, and finally diopside. Minor Al,Ti-rich diopside occurs interstitially to spinel (Figs. 7c, d), suggesting its metastable formation after hibonite and before or with spinel. This is inconsistent with thermodynamic equilibrium condensation models that predict that Al,Ti-rich diopside condenses as the first composition of pyroxene after spinel and melilite (Ebel, 2006). Like the majority of hibonite-rich CAIs in ALHA77307 (Russell et al., 1998; Han et al., 2015), melilite is completely absent, which is also inconsistent with thermodynamic equilibrium condensation models that predict that melilite condenses after hibonite and before spinel and diopside (Ebel, 2006). These inconsistencies between the observed and predicted formation sequence of spinel, melilite, and Al,Ti-rich diopside may have arisen as the result of disequilibrium condensation from a super-cooled nebular gas (Petaev and Wood, 2005). In addition, hibonite is embayed by spinel, in which most grains are elongated normal to the *c** axis of hibonite (Figs. 7c, d). The crystallographic orientation relationships between hibonite and spinel (Fig. 8) were found from CAI 2–119, as well as from similar hibonite-rich inclusions from ALHA77307 (Han et al., 2015) and from the Murchison and Paris CM chondrites (Han et al., 2017). According to the crystal structures of hibonite and spinel indexed from diffraction patterns in Figure 8, the (111) plane of spinel consists of a hexagonalclose-packed array of oxygen ions with Al in octahedral sites, which resembles the oxygen arrangement in the (001) plane of hexagonal-structured hibonite. These lines of evidence suggest that epitaxial nucleation and growth of spinel on hibonite was favored by a structural similarity between the two phases, which enabled the direct replacement reaction of hibonite and gaseous Mg by spinel (Beckett and Stolper, 1994; Han et al., 2015). Instead,

melilite condensation was kinetically inhibited after hibonite (Beckett and Stolper, 1994; Han et al., 2015), resulting in the complete lack of melilite in hibonite-rich inclusions in ALHA77307 including CAI 2–119, as well as in CM chondrites (Simon et al., 2006). Suppression of melilite condensation could have produced excess Ca in the gas phase (i.e., supersaturation), which kinetically stabilized diopside after spinel by taking up Ca in the gas phase. As a final step, diopside formed onto spinel by reaction of spinel with a gas where Mg, Si, and Ca with minor Ti had not already condensed. As discussed above, Al and Ti were readily incorporated into diopside, forming minor Al,Ti-rich diopside as the first composition, followed by condensation of pure diopside (Han and Brearley, 2016).

Interestingly, all three CAIs 05, 1–65, and 2–119 lack anorthite, which commonly replaces melilite in CAIs and amoeboid olivine aggregates in carbonaceous chondrites. Thermodynamic equilibrium condensation models predict that anorthite condenses after spinel, pyroxene, and olivine (Ebel, 2006). The simplest explanation is that the inclusions did not remain in contact with a nebular gas at temperatures where anorthite begins to condense (~1,420 K at $P^{tot} = 10^{-3}$ atm; Ebel, 2006), prohibiting an anorthite-forming reaction of melilite and a nebular gas (Petaev and Wood, 2005). The common occurrence of a diopside rim on the exterior of fine-grained inclusions in ALHA77307 (Figs. 1, 3, 6) and in other carbonaceous chondrites suggests that condensation of pyroxene was kinetically favored instead of anorthite under disequilibrium conditions. The diopside rim normally shows the zonal sequence of Al,Ti-rich > Al-rich, Ti-poor > Al,Ti-poor towards the inclusion core, despite differences in its thickness and compositional range (Han and Brearley, 2017; this study). We therefore infer that many inclusions experienced a very similar final stage to form zoned diopside by a reaction of spinel and melilite with a gas where Ti, Mg, and SiO had not completely condensed yet, but preserve evidence of distinct formation processes and conditions for each of their primary core assemblages (hibonite, perovskite, spinel, and/or melilite).

4.2. CAI 2–112: Igneous Inclusion

The observed texture and mineral assemblage of CAI 2–112 (Fig. 10) are consistent with an igneous origin; spinel crystallized first from a refractory melt, followed by melilite, as experimentally demonstrated by Stolper (1982). The melt origin of this CAI is also inferred by its textural similarities to compact type A CAIs in CV3 chondrites where subhedral to euhedral spinel grains are poikilitically enclosed in melilite, most of which are gehlenitic with $Åk_{<\sim 45}$ (Simon et al., 1999). The presence of very gehlenitic melilite ($Åk_{5–15}$) with its observed zonation (Fig. 10c) may reflect the compositional evolution of melilite crystallized from a refractory melt during cooling from very high temperatures; melilite may have begun to crystallize at temperatures higher than 1,500°C and become more åkermanatic with decreasing temperature down to ~1,450°C (Stolper, 1982; Grossman et al., 2002; Mendybaev et al., 2006). At such high temperatures, some degree of evaporation may also have produced a relative depletion in Mg and Si from the surface of a molten CAI precursor, and more gehlenitic melilite would have crystallized preferentially there (Mendybaev et al., 2006).

4.3. ^{16}O-Rich Fine-Grained CAIs in ALHA77307

Our oxygen isotope data of the fine-grained CAIs in ALHA77307, together with their mineralogy and petrology, suggest that they originally formed and evolved in a common ^{16}O-rich gas reservoir over a large temperature interval. Melilite in CAIs 05 and 2–112 are consistently ^{16}O-rich (Δ^{17}O <−19‰) and isotopically indistinguishable from spinel in the same inclusions (Fig. 11; Table 2). This supports the well-established view that fine-grained CAIs in CO3.0 chondrites, including ALHA77307, retain primary ^{16}O-rich compositions with Δ^{17}O ranging from −30‰ to −20‰ (Wasson et al., 2001; Itoh et al., 2004; Ushikubo et al., 2017; Simon et al. 2019a, b), which may have reflected the local heterogeneity in the CAI-forming reservoir (e.g., Yurimoto et al., 1998; Young and Russell, 1998; Simon et al., 2011, 2016). The pristine nature of the ALHA77307 CAIs studied is also supported by the presence of highly refractory phases with no or little Fe and Na enrichments and the complete absence of secondary alteration phases such as nepheline or sodalite that are commonly observed in CAIs from metamorphosed CO and CV chondrites (Brearley and Krot, 2013), even down to the TEM scale (Han et al., 2015; Han and Brearley, 2017). In contrast, fluid-assisted thermal metamorphism in the parent body setting results in appreciable enrichments in heavy oxygen isotopes in melilite and anorthite, relative to spinel and pyroxene (e.g., Wasson et al., 2001; Fagan et al., 2004; Itoh et al., 2004; Aléon et al., 2005; Simon et al., 2019b; Krot et al., 2019). For example, melilite in almost all CAIs in Kainsaz (CO3.2) and Ornans (CO3.3) has Δ^{17}O >−15‰, which is well correlated with its FeO contents (Wasson et al., 2001).

The rare CAI 2–112 is an igneous inclusion that shows petrologic evidence for melting. However, this inclusion is isotopically uniform with an average Δ^{17}O value of ~−22.6±5.0‰ (Fig. 11; Table 2), very similar to other ALHA77307 CAIs analyzed in this study that most likely represent condensation products. Wasson et al. (2001) also reported ^{16}O-rich compositions (Δ^{17}O = −30‰ to −26‰) of spinel and melilite from a melilite-rich CAI C1 in Colony (CO3.0) whose textural characteristics were interpreted as crystallization from a partial melt. Therefore, we infer a similar ^{16}O-rich gas reservoir during the formation of these two igneous inclusions, as inferred for other fine-grained CAIs in ALHA77307 analyzed in this study. Such ^{16}O-rich compositions may have been inherited from precursor CAIs that were originally ^{16}O-rich and never experienced a significant oxygen isotope exchange with the surrounding nebular gas during a subsequent melting event or events. An exception is given by Itoh et al. (2004) who observed a poikilitic texture of CAI Y20–1 in Yamato 81020 (CO3.0) with an ^{16}O-rich spinel relict (Δ^{17}O = −21‰) enclosed in ^{16}O-depleted diopside and anorthite (Δ^{17}O = −12‰ to −8‰). These heterogeneous oxygen isotopic compositions were inferred as evidence for an oxygen isotope exchange between an ^{16}O-rich, partially molten precursor and an ^{16}O-poor gas. Collectively, these observations suggest that fine-grained CAIs in CO3.0 chondrites formed by condensation in a primary ^{16}O-rich gas reservoir, but some experienced later, episodic melting event(s) in reservoirs of different oxygen isotopic compositions that caused various degrees of oxygen isotopic exchange. Aléon et al. (2002) reached a similar conclusion based on the apparent correlation between the oxygen isotopic compositions of fine-grained CAIs in CR chondrites and their textural type: most igneous CAIs are relatively ^{16}O-poor (Δ^{17}O = −18‰ to −3‰), whereas most other CAIs interpreted as condensates are uniformly ^{16}O-rich (Δ^{17}O ≤−22‰). In

particular, two melilite-rich inclusions 18–2 and −3 from the Graves Nunataks 95229 CR2 chondrite that have textural and mineralogical similarities to CAI 2–112 from ALHA77307 have relatively ^{16}O-depleted compositions (Δ^{17}O = −14‰ and −18‰, respectively; Aléon et al., 2002). Such ^{16}O-poor isotopic compositions of igneous CAIs are most likely a later overprint that resulted from melting of originally ^{16}O-rich CAIs in a relatively ^{16}O-poor nebular gas, as inferred for some coarse-grained Type B CAIs in CV3 chondrites (e.g., Yurimoto et al., 1998; Fagan et al., 2004; Yoshitake et al., 2005; Aléon, 2016; Kawasaki et al., 2018).

Complex oxygen isotopic zoning across CAIs and their rims in CV3 chondrites has been observed in several studies (e.g., Yoshitake et al., 2005; Ito et al., 2010; Needham et al., 2015; Simon et al., 2011, 2016). However, the mechanism(s) and environment responsible for this internal oxygen isotope heterogeneity remain controversial. These variations may be attributable to high-temperature nebular processing involving both ^{16}O-rich and ^{16}O-poor gas reservoirs (e.g., Simon et al., 2011, 2016) or to low-temperature parent body processing involving ^{16}O-poor aqueous fluids (e.g., Bodénan et al., 2014; Krot et al., 2017; Krot et al., 2019) due to pervasive parent body metasomatic and metamorphic effects on CV3 CAIs (Brearley and Krot, 2013). The uniformity of oxygen isotopic compositions across the interior and rim of least-altered, fine-grained CAIs from CM, CO, CR, CH, and Acfer 094 chondrites (Matzel et al., 2013; Bodénan et al., 2014; Krot et al., 2017; Ushikubo et al., 2017; this study) clearly indicates that an ^{16}O-rich gas reservoir(s) existed during the entire period of formation of these CAIs and their rims. However, there are significant variations in mineralogy and complexity of rims among CAIs, indicative of their different formation processes and conditions. For example, fine-grained CAIs in CO3 chondrites have a simple rim composed predominantly of zoned diopside (Russell et al., 1998; Han and Brearley, 2017), compared to some CV3 CAIs that have a well-developed sequence of successive monomineralic layers composed at least of spinel, melilite, and zoned diopside (Wark and Lovering, 1977). Additional studies are therefore required to evaluate if primordial rims on individual CAIs from different chondrite groups commonly share the same, homogeneous ^{16}O-rich signature.

5. CONCLUSIONS

We conducted a coordinated analysis of mineralogy, petrology, and oxygen isotopic compositions of four fine-grained CAIs in ALHA77307 that represent three major groups, melilite-rich, spinel-rich, and hibonite-rich, in CO3 chondrites based on their primary core mineralogy (Russell et al., 1998; Simon and Grossman, 2015; Han and Brearley, 2017). The observed difference in the primary core mineralogy of the ALHA77307 CAIs studied indicate that each of these inclusions reflects unique nebular environments in which multiple high-temperature processes occurred during the formation of primary core mineral assemblages. The three CAIs 05, 1–65, and 2–119 are interpreted as fine-grained aggregates of high-temperature nebular condensates that formed under non-equilibrium conditions, whereas CAI 2–112 appears to represent fragments of a larger melilite-rich inclusion that crystallized from a refractory melt. Previous trace element and isotopic studies of fine-grained CAIs in CO3 chondrites provide additional support for their common condensation origin (Fahey et al., 1994; Russell et al., 1998). However, fine-grained inclusions with

distinct igneous textures such as CAI 2–112 are extremely rare in CO3 chondrites, suggesting that most CAIs incorporated into the CO3 chondrite parent body escaped later thermal processing such as melting and evaporation.

Despite their mineralogical and textural differences, all four fine-grained CAIs in ALHA77307 are uniformly ^{16}O-rich, with an average Δ^{17}O value of ~−22‰, suggesting a prevalent ^{16}O-rich gas reservoir throughout their formation. However, evidence for an oxygen isotopic exchange between a ^{16}O-rich, partially molten precursor and a ^{16}O-poor nebular gas was inferred from a single inclusion from Yamato 81020 (Itoh et al., 2004). This suggests that fine-grained CAIs in CO3 chondrites formed in a primary ^{16}O-rich gas reservoir, but a few of them interacted with gas reservoir(s) of different oxygen isotopic compositions during the course of transport of refractory precursors or evolution of a gas reservoir surrounding refractory precursors.

ACKNOWLEDGMENTS

We thank Dr. Noriyuki Kawasaki and an anonymous reviewer for their constructive reviews and Dr. Alexander Krot for his editorial handling. We gratefully acknowledge the access to the Electron Microbeam Analysis Facility at Department of Earth and Planetary Sciences and Institute of Meteoritics, University of New Mexico and at Astromaterials Research and Exploration Science Division, NASA Johnson Space Center. This work was supported by NASA grants 17-EW17_2-0148 (L.P.K.), NNG06GG37G, NNX12AH59G, and NNX15AD28G (A.J.B.), and 80NSSC18K0602 (M.-C.L.). The UCLA ion microprobe facility is partially supported by a grant from the NSF Instrumentation and Facilities program. The work performed at Lawrence Livermore National Laboratory (B.J. & J.E.M) was supported by NASA grants NNH10AO05I and NNH10AO48I and by the Laboratory Directed Research and Development grant 17-ERD-001. This work was performed under the auspices of the U.S. Department of Energy by Lawrence Livermore National Laboratory under Contract DE-AC52-07NA27344. LPI contribution No. 2223.

REFERENCES

Aléon J, 2016 Oxygen isotopes in the early protoplanetary disk inferred from pyroxene in a classical type B CAI. Earth Planet. Sci. Lett 440, 62–70.

Aléon J, Krot AN, McKeegan KD, 2002 Calcium-aluminum-rich inclusions and amoeboid olivine aggregates from the CR carbonaceous chondrites. Meteorit. Planet. Sci 37, 1729–1755.

Aléon J, Krot AN, McKeegan KD, MacPherson GJ, Ulyanov AA, 2005 Fine-grained, spinel-rich inclusions from the reduced CV chondrite Efremovka: II. Oxygen isotopic compositions. Meteorit. Planet. Sci 40, 1043–1058.

Beckett JR, Stolper E, 1994 The stability of hibonite, melilite, and other aluminous phases in silicate melts: Implications for the origin of hibonite-bearing inclusions from carbonaceous chondrites. Meteoritics 29, 41–65.

Bodénan J-D, Starkey NA, Russell SS, Wright IP, Franchi IA, 2014 An oxygen isotope study of Wark–Lovering rims on type A CAIs in primitive carbonaceous chondrites. Earth Planet. Sci. Lett 401, 327–336.

Boss AP, Alexander CMO'D, Podolak M, 2012 Cosmochemical consequences of particle trajectories during FU Orionis outbursts by the early Sun. Earth Planet. Sci. Lett 345–348, 18–26.

Brearley AJ, Krot AN, 2013 Metasomatism in the early solar system: the record from chondritic meteorites In Metasomatism and the Chemical Transformation of Rock (eds. Harlov DE and Austrheim A). Springer, Berlin Heidelberg, pp. 659–789.

Ciesla FJ, 2010 The distributions and ages of refractory objects in the solar nebula. Icarus 208, 455–467.

Clayton RN, Onuma N, Grossman L, Mayeda TK, 1977 Distribution of the pre-solar component in Allende and other carbonaceous chondrites. Earth Planet. Sci. Lett 34, 209–224.

Connelly JN, Bizzarro M, Krot AN, Nordlund Å, Wielandt D, Ivanova MA, 2012 The absolute chronology and thermal processing of solids in the solar protoplanetary disk. Science 338, 651–655. [PubMed: 23118187]

Ebel DS, 2006 Condensation of rocky material in astrophysical environments In Meteorites and the Early Solar System II (eds. Lauretta DS and McSween HY Jr.). University of Arizona Press, Tucson, pp. 253–277.

Fagan TJ, Krot AN, Keil K, Yurimoto H, 2004 Oxygen isotopic alteration in Ca-Al-rich inclusions from Efremovka: Nebular or parent body setting? Meteorit. Planet. Sci 39, 1257–1272.

Fahey AJ, Zinner EK, Kurat G, Kracher A, 1994 Hibonite-hercynite inclusion HH-1 from the Lance (CO3) meteorite: The solar nebula processing of an ultra-refractory CAI. Geochim. Cosmochim. Acta 58, 4779–4793.

Grossman JN, Brearley AJ, 2005 The onset of metamorphism in ordinary and carbonaceous chondrites. Meteorit. Planet. Sci 40, 87–122.

Grossman L, Ebel DS, Simon SB, Davis AM, Richter FM, Parsad NM, 2000 Major element chemical and isotopic compositions of refractory inclusions in C3 chondrites: the separate roles of condensation and evaporation. Geochim. Cosmochim. Acta 64, 2879–2894.

Grossman L, Ebel DS, Simon SB, 2002 Formation of refractory inclusions by evaporation of condensate precursors. Geochim. Cosmochim. Acta 66, 145–161.

Han J, Brearley AJ, 2016 Microstructural constraints on complex thermal histories of refractory CAI-like objects in an amoeboid olivine aggregate from the ALHA77307 CO3.0 chondrite. Geochim. Cosmochim. Acta 183, 176–197.

Han J, Brearley AJ, 2017 Microstructures and formation history of melilite-rich calcium–aluminum-rich inclusions from the ALHA77307 CO3.0 chondrite. Geochim. Cosmochim. Acta 201, 136–154.

Han J, Brearley AJ, Keller LP, 2015 Microstructural evidence for a disequilibrium condensation origin for hibonite-spinel inclusions in the ALHA77307 CO3.0 chondrite. Meteorit. Planet. Sci 50, 2121–2136.

Han J, Liu M-C, Kööp L, Keller LP, Davis AM, 2017 Correlations among microstructure, morphology, chemistry, and isotopic systematics of hibonite in CM chondrites (abstract). 80th Annual Meeting of the Meteoritical Society, 6380.

Ito M, Messenger S, Keller LP, Rahman ZU, Ross DK, Nakamura-Messenger K, 2010 FIB-NanoSIMS-TEM coordinated study of a Wark-Lovering rim in a Vigarano type A CAI (abstract). Lunar Planet. Sci 41, 1177.

Itoh S, Kojima H, Yurimoto H, 2004 Petrography and oxygen isotopic compositions in refractory inclusions from CO chondrites. Geochim. Cosmochim. Acta 68, 183–194.

Kawasaki N, Itoh S, Sakamoto N, Yorimoto H, 2017 Chronological study of oxygen isotope composition for the solar protoplanetary disk recorded in a fluffy Type A CAI from Vigarano. Geochim. Cosmochim. Acta 201, 83–102.

Kawasaki N, Simon SB, Grossman L, Sakamoto N, Yurimoto H, 2018 Crystal growth and disequilibrium distribution of oxygen isotopes in an igneous Ca-Al-rich inclusion from the Allende carbonaceous chondrite. Geochim. Cosmochim. Acta 221, 318–341.

Keller LP, Needham AW, Messenger S, 2013 A FIB/TEM study of a complex Wark-Lovering rim on a Vigarano CAI (abstract). 76th Annual Meteoritical Society Meeting, 5300.

Kobatake H, Tsukamoto K, Nozawa J, Nagashima K, Satoh H, Dold P, 2008 Crystallization of cosmic dust from highly supersaturated silicate vapor in a rapidly cooled environment. Icarus 198, 208–217.

Krot AN, MacPherson GJ, Ulyanov AA, Petaev MI, 2004a Fine-grained, spinel-rich inclusions from the reduced CV chondrites Efremovka and Leoville: I. Mineralogy, petrology, and bulk chemistry. Meteorit. Planet. Sci 39, 1517–1553.

Krot AN, Petaev MI, Russell SS, Itoh S, Fagan T, Yurimoto H, Chizmadia L, Weisberg MK, Komatsu M, Ulyanov AA, Keil K, 2004b Amoeboid olivine aggregates in carbonaceous chondrites: records of nebular and asteroidal processes. (Invited review). Chem. Erde 64, 185–239.

Krot AN, Nagashima K, van Kooten EMM, Bizzarro M, 2017 High-temperature rims around calcium–aluminum-rich inclusions from the CR, CB, and CH carbonaceous chondrites. Geochim. Cosmochim. Acta 201, 155–184.

Krot AN, Nagashima K, Fintor K, Pál-Molnár E, 2019 Evidence for oxygen-isotope exchange in refractory inclusions from Kaba (CV3.1) carbonaceous chondrite during fluid-rock interaction on the CV parent asteroid. Geochim. Cosmochim. Acta, 246, 419–435.

MacPherson GJ, 2014 Calcium-aluminum-rich inclusions in chondritic meteorites In Meteorites, Comets and Planets, vol. 1 (ed. Davis AM) Treatise on Geochemistry (eds. Holland HD and Turekian KK). Elsevier, Oxford pp. 201–246.

MacPherson GJ, Grossman L, 1981 A once-molten, coarse-grained, Ca-rich inclusion in Allende. Earth Planet. Sci. Lett 52, 16–24.

MacPherson GJ, Bar-Matthews M, Tanaka T, Olsen E, Grossman L, 1983 Refractory inclusions in the Murchison meteorite. Geochim. Cosmochim. Acta 47, 823–839.

Matzel JEP, Simon JI, Hutcheon ID, Jacobsen B, Simon SB, Grossman L, 2013 Oxygen isotope measurements of a rare Murchison type A CAI and its rim (abstract). Lunar Planet. Sci 44, 2632.

Mendybaev RA, Richter FM, Davis AM, 2006 Crystallization of melilite from CMAS-liquids and the formation of the melilite mantle of Type B1 CAIs: Experimental simulations. Geochim. Cosmochim. Acta 70, 2622–2642.

Needham AW, Messenger S, Keller LP, Simon JI, Han J, Mishra RK, 2015 Systematic oxygen isotope variations within a single Vigarano CAI surrounded by a uniformly ^{16}O-rich Wark-Lovering rim (abstract). Lunar Planet. Sci 46, 2865.

Needham AW, Messenger S, Han J, Keller LP, 2017 Corundum–hibonite inclusions and the environments of high temperature processing in the early Solar System. Geochim. Cosmochim. Acta 196, 18–35.

Nozawa J, Tsukamoto K, Kobatake H, Yamada J, Satoh H, Nagashima K, Miura H, Kimura Y, 2009 AFM study on surface nanotopography of matrix olivines in Allende carbonaceous chondrite. Icarus 204, 681–686.

Russell SS, Huss GR, Fahey AJ, Greenwood RC, Hutchison R, Wasserburg GJ, 1998 An isotopic and petrologic study of calcium-aluminum-rich inclusions from CO3 meteorites. Geochim. Cosmochim. Acta 62, 689–714.

Ryerson FJ, McKeegan KD, 1994 Determination of oxygen self-diffusion in akermanite, anorthite, diopside, and spinel: implications for oxygen isotopic anomalies and the thermal histories of Ca–Al-rich inclusions. Geochim. Cosmochim. Acta 58, 3713–3734.

Park C, Wakaki S, Sakamoto N, Kobayashi S, Yurimoto H, 2012 Oxygen isotopic composition of the solar nebula gas inferred from high-precision isotope imaging of melilite crystals in an Allende CAI. Meteorit. Planet. Sci 47, 2070–2083.

Petaev MI, Wood JA, 2005 Meteoritic constraints on temperatures, pressures, cooling rates, chemical compositions, and modes of condensation in the solar nebula. In Chondrites and the protoplanetary disk, edited by Krot AN, Scott ERD and Reipurth B ASP conference series. 341. San Francisco: Astronomical Society of the Pacific pp. 373–406.

Simon JI, Hutcheon ID, Simon SB, Matzel JEP, Ramon EC, Weber PK, Grossman L, DePaolo DJ, 2011 Oxygen isotope variations at the margin of a CAI records circulation within the solar nebula. Science 331, 1175–1178. [PubMed: 21385711]

Simon JI, Matzel JEP, Simon SB, Hutcheon ID, Ross DK, Weber PK, Grossman L, 2016 Oxygen isotopic variations in the outer margins and Wark–Lovering rims of refractory inclusions. Geochim. Cosmochim. Acta 186, 242–276.

Simon SB, Grossman L, 2015 Refractory inclusions in the pristine carbonaceous chondrites DOM 08004 and DOM 08006. Meteorit. Planet. Sci 50, 1032–1049.

Simon SB, Davis AM, Grossman L, 1999 Origin of compact Type A refractory inclusions from CV3 carbonaceous chondrites. Geochim. Cosmochim. Acta 63, 1233–1248.

Simon SB, Grossman L, Hutcheon ID, Phinney DL, Weber PK, Fallon SJ, 2006 Formation of spinel-, hibonite-rich inclusions found in CM2 carbonaceous chondrites. Am. Mineral 91, 1675–1687.

Simon SB, Krot AN, Nagashima K, Kööp L, Davis AM, 2019a Condensate refractory inclusions from the CO3.00 chondrite Dominion Range 08006: Petrography, mineral chemistry, and isotopic compositions. Geochim. Cosmochim. Acta 246, 109–122. [PubMed: 30846886]

Simon SB, Krot AN, Nagashima K, 2019b Oxygen and Al-Mg isotopic compositions of grossite-bearing refractory inclusions from CO3 chondrites. Meteorit. Planet. Sci 54, 1362–1378.

Stolper E, 1982 Crystallization sequences of Ca–Al-rich inclusions from Allende: an experimental study. Geochim. Cosmochim. Acta 46, 2159–2180.

Ushikubo T, Kimura M, Kita NT, Valley JW, 2012 Primordial oxygen isotope reservoirs of the solar nebula recorded in chondrules in Acfer 094 carbonaceous chondrite. Geochim. Cosmochim. Acta 90, 242–264.

Ushikubo T, Tenner TJ, Hiyagon H, Kita NT, 2017 A long duration of the ^{16}O-rich reservoir in the solar nebula, as recorded in fine-grained refractory inclusions from the least metamorphosed carbonaceous chondrites. Geochim. Cosmochim. Acta 201, 103–122.

Wark D, Lovering JF, 1977 Marker events in the early evolution of the solar system: evidence from rims on Ca–Al-rich inclusions in carbonaceous chondrites. Proc. Lunar Planet. Sci. Conf 8, 95–112.

Wasson JT, Yurimoto H, Russell SS, 2001 ^{16}O-rich melilite in CO3.0 chondrites: Possible formation of common, ^{16}O-poor melilite by aqueous alteration. Geochim. Cosmochim. Acta 65, 4539–4549.

Yoneda S, Grossman L, 1995 Condensation of CaO–MgO–Al_2O_3–SiO_2 liquids from cosmic gases. Geochim. Cosmochim. Acta 59, 3413–3444.

Yoshitake M, Koide Y, Yurimoto H, 2005 Correlations between oxygen-isotopic composition and petrologic setting in a coarse-grained Ca, Al–rich inclusion. Geochim. Cosmochim. Acta 69, 2663–2674.

Young ED, Russell SS, 1998 Oxygen reservoirs in the early solar nebula inferred from an Allende CAI. Science 282, 452–455.

Yurimoto H, Ito M, Nagasawa H, 1998 Oxygen isotope exchange between refractory inclusion in Allende and solar nebula gas. Science 282, 1874–1877.

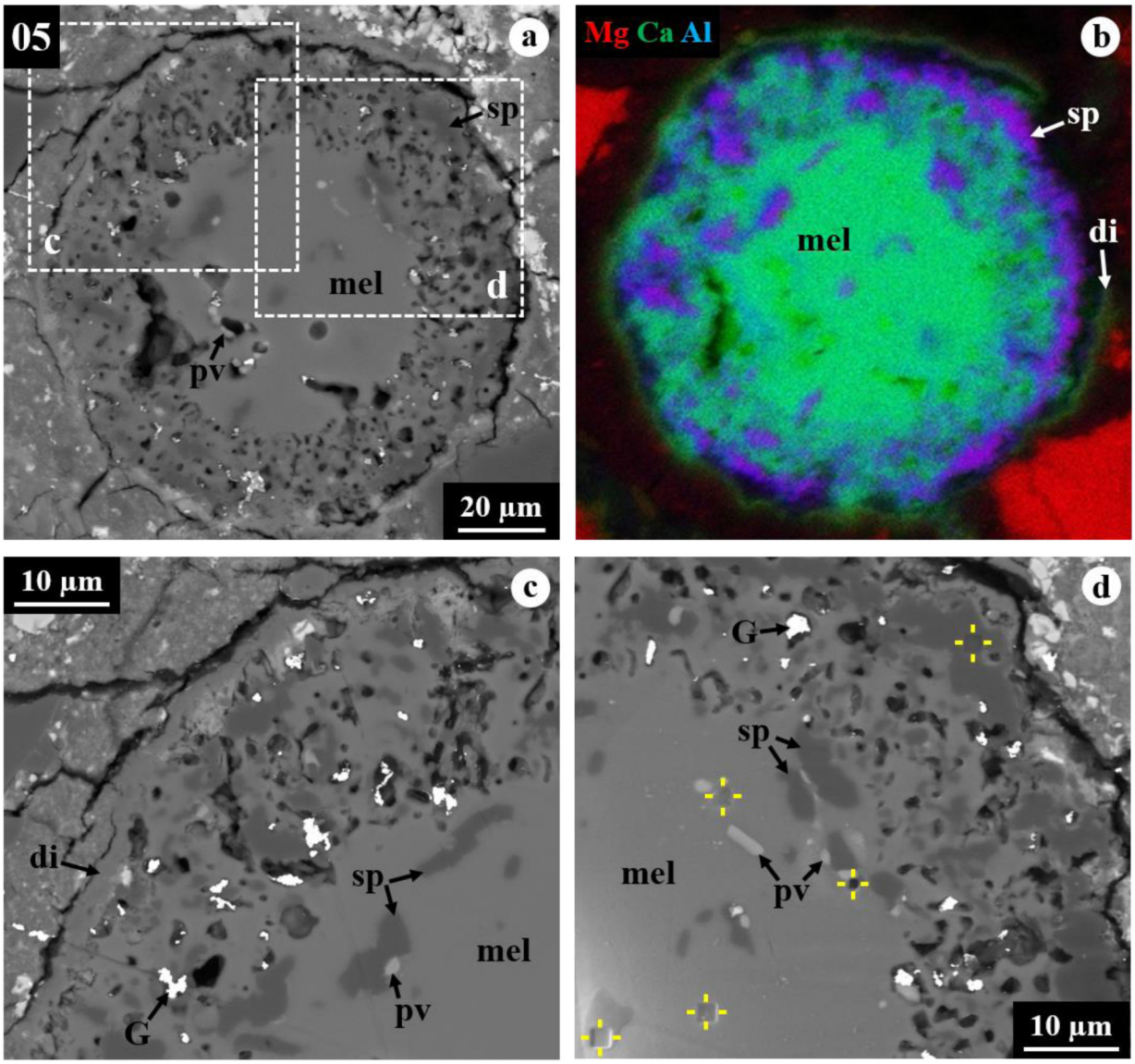

Figure 1.

BSE images (a, c, d) and combined x-ray map (b) in Mg Kα in red, Ca Kα in green, and Al Kα in blue of melilite-rich CAI 05 from ALHA77307. The regions outlined in (a) are shown in detail in (c, d). This inclusion has a distinct zonal structure that consists of a compact melilite-rich core completely enclosed by a porous mantle, rimmed by a discontinuous layer of diopside. Hereafter, NanoSIMS spots measured for O isotopes are indicated by yellow solid lines. Abbreviations hereafter: hib = hibonite, pv = perovskite, sp = spinel, mel = melilite, di = diopside, fo = forsterite, mx = matrix; G = gold coating residues, p=pore.

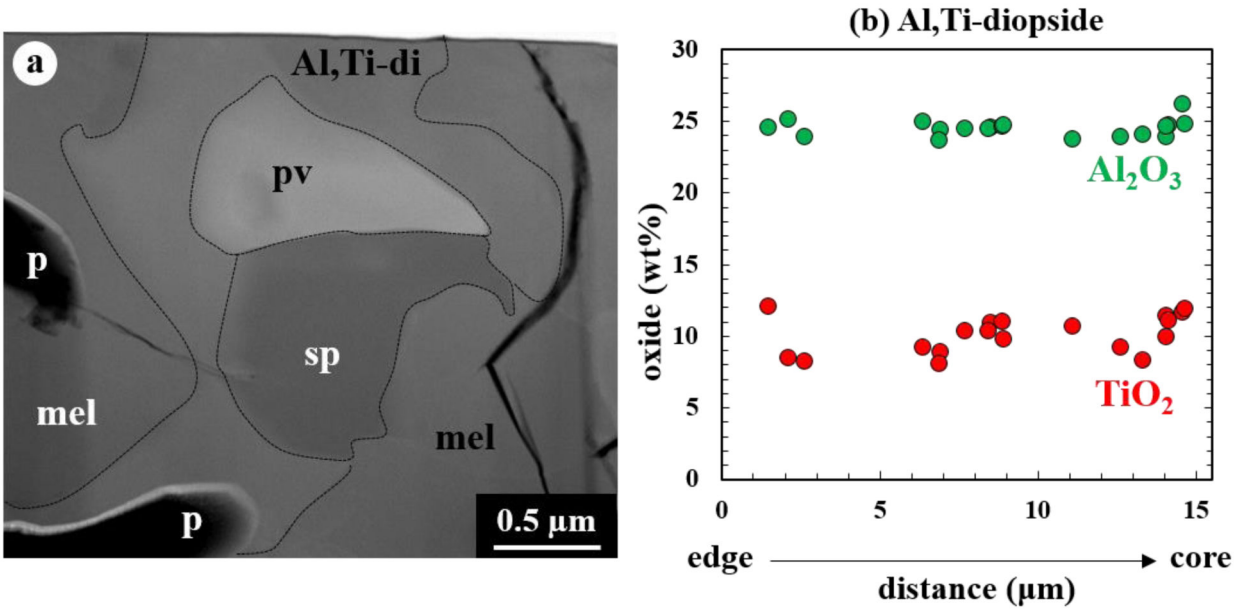

Figure 2.

(a) DF-STEM image of a perovskite grain enclosed by an intergrowth of Al,Ti-rich diopside, spinel, and melilite in the mantle of CAI 05. All phases are highly irregular. Pores are present throughout the mantle and concentrated in melilite. Each phase is outlined by dotted lines. (b) Variations of Al_2O_3 and TiO_2 contents (in wt%) in pyroxene from the mantle that is consistently Al,Ti-rich. Individual points represent single TEM EDX analyses obtained from pyroxene grains present throughout the entire FIB section. A distance of 0 µm corresponds to the outermost edge of the inclusion.

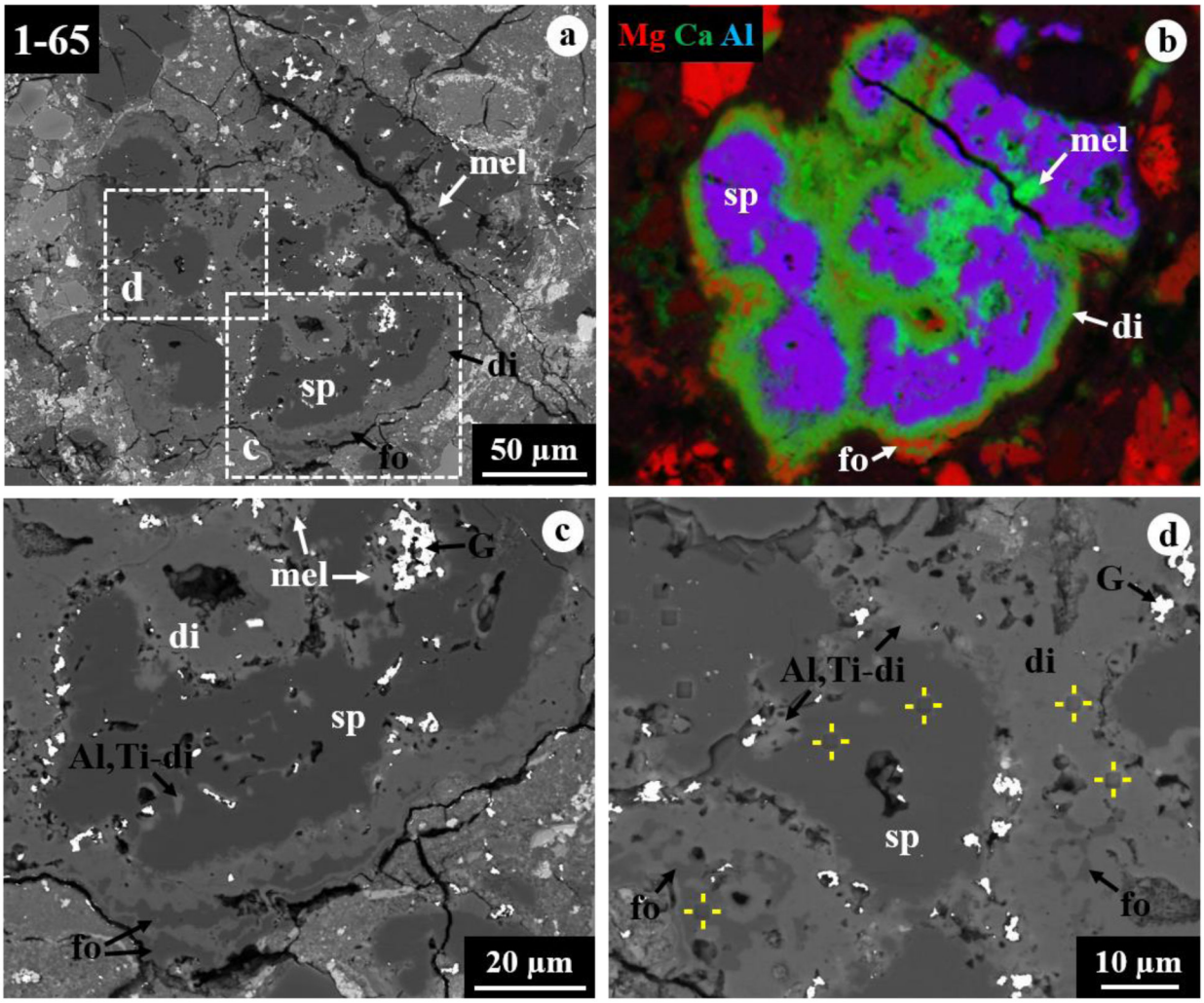

Figure 3.

BSE images (a, c, d) and combined x-ray map (b) in Mg Kα in red, Ca Kα in green, and Al Kα in blue of spinel-rich CAI 1–65 from ALHA77307. The regions outlined in (a) are shown in detail in (c, d). This CAI is a mineralogically-zoned inclusion consisting of nodules of spinel cores corroded by layers of Al,Ti-rich diopside and minor melilite, finally rimmed by diopside with minor forsterite.

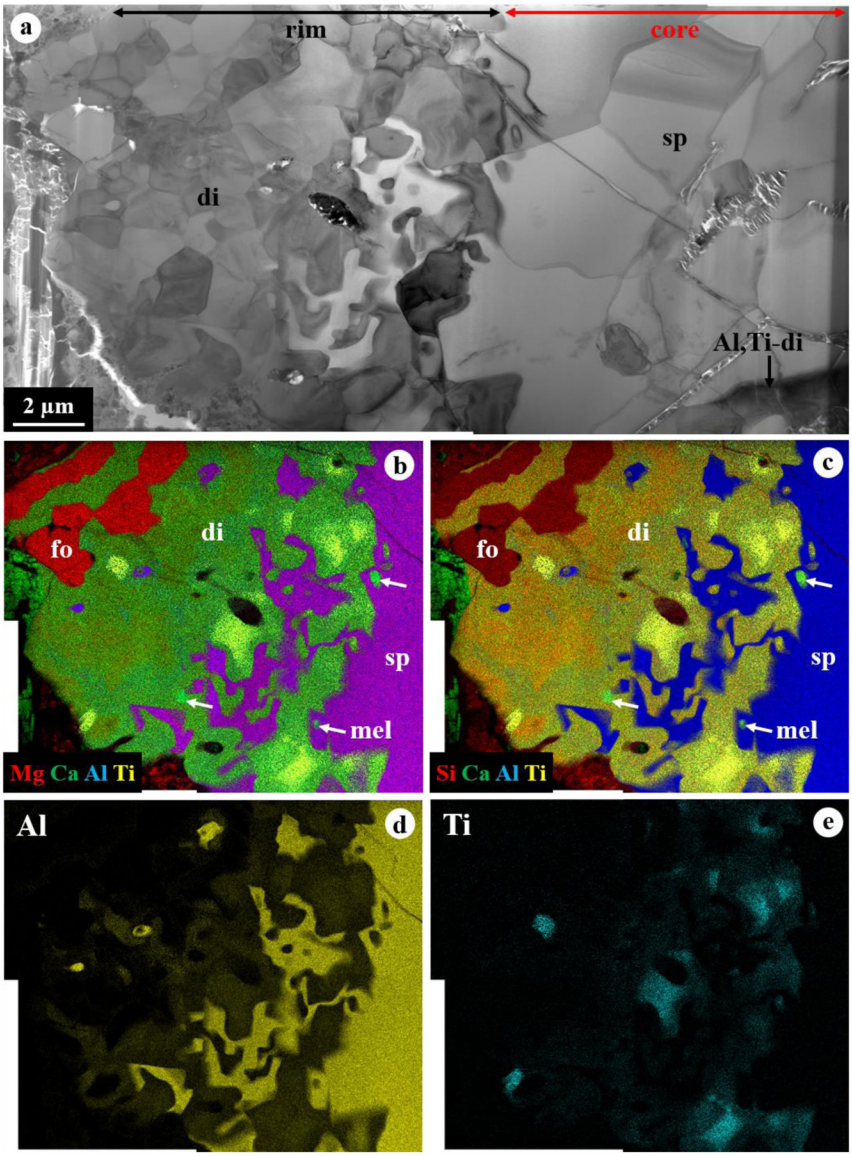

Figure 4.

TEM images of a FIB section from CAI 1–65. (a) BF-STEM image and (b, c) combined TEM EDX maps of the FIB section that shows a complex zonal sequence from the spinel core, intergrowth of spinel + Al,Ti-rich diopside + minor melilite, Al-rich diopside with minor spinel and Al,Ti-rich diopside, forsterite, diopside, forsterite, to diopside. (d, e) Elemental Al and Ti map obtained using TEM EDX, revealing the Al and Ti zonation in pyroxene.

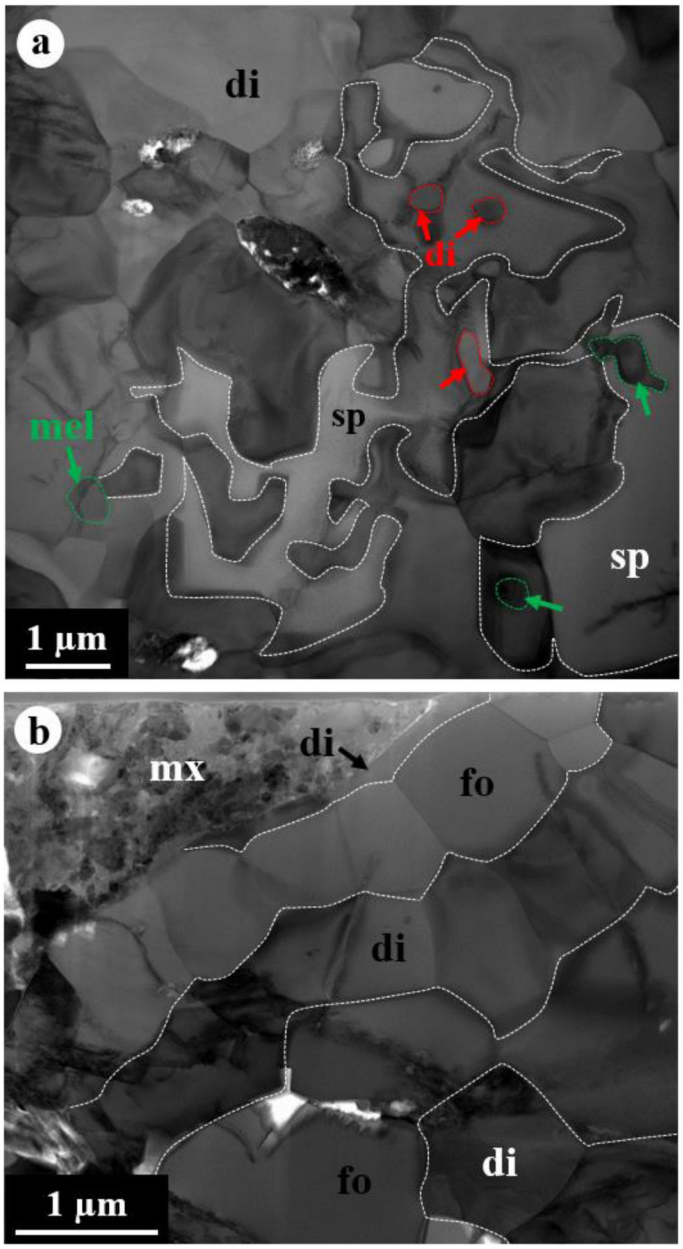

Figure 5.

BF-STEM images of (a) the intergrowth layer of spinel + Al,Ti-rich diopside + melilite and (b) the outermost rim of diopside + forsterite in CAI 1–65. The intergrowth layer at the interface with the spinel core shows highly unequilibrated grain boundary microstructures, in contrast to the outermost rim having equilibrated grain boundary microstructures. Each phase is outlined by dotted lines. In (a), diopside grains enclosed by spinel are outlined by red dotted lines, and melilite grains are outlined by green dotted lines.

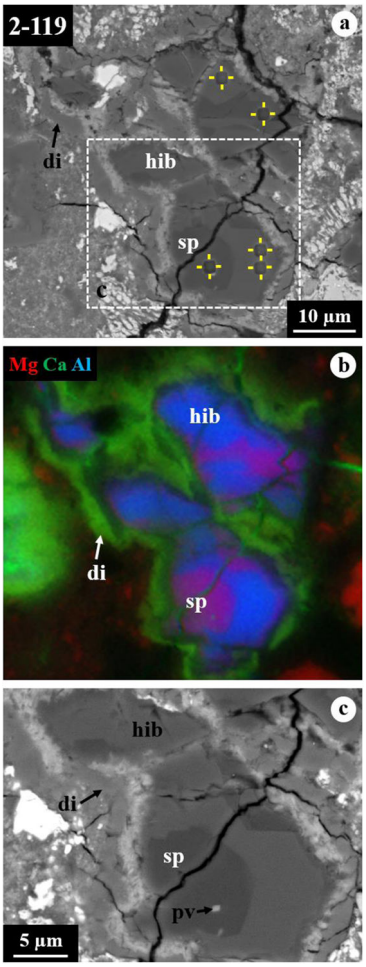

Figure 6.

BSE images (a, c) and combined x-ray map (b) in Mg Kα in red, Ca Kα in green, and Al Kα in blue of hibonite-rich CAI 2–119 from ALHA77307. The regions outlined in (a) are shown in detail in (c). In this CAI, individual nodules consist of hibonite grains partially to completely surrounded by spinel with minor perovskite.

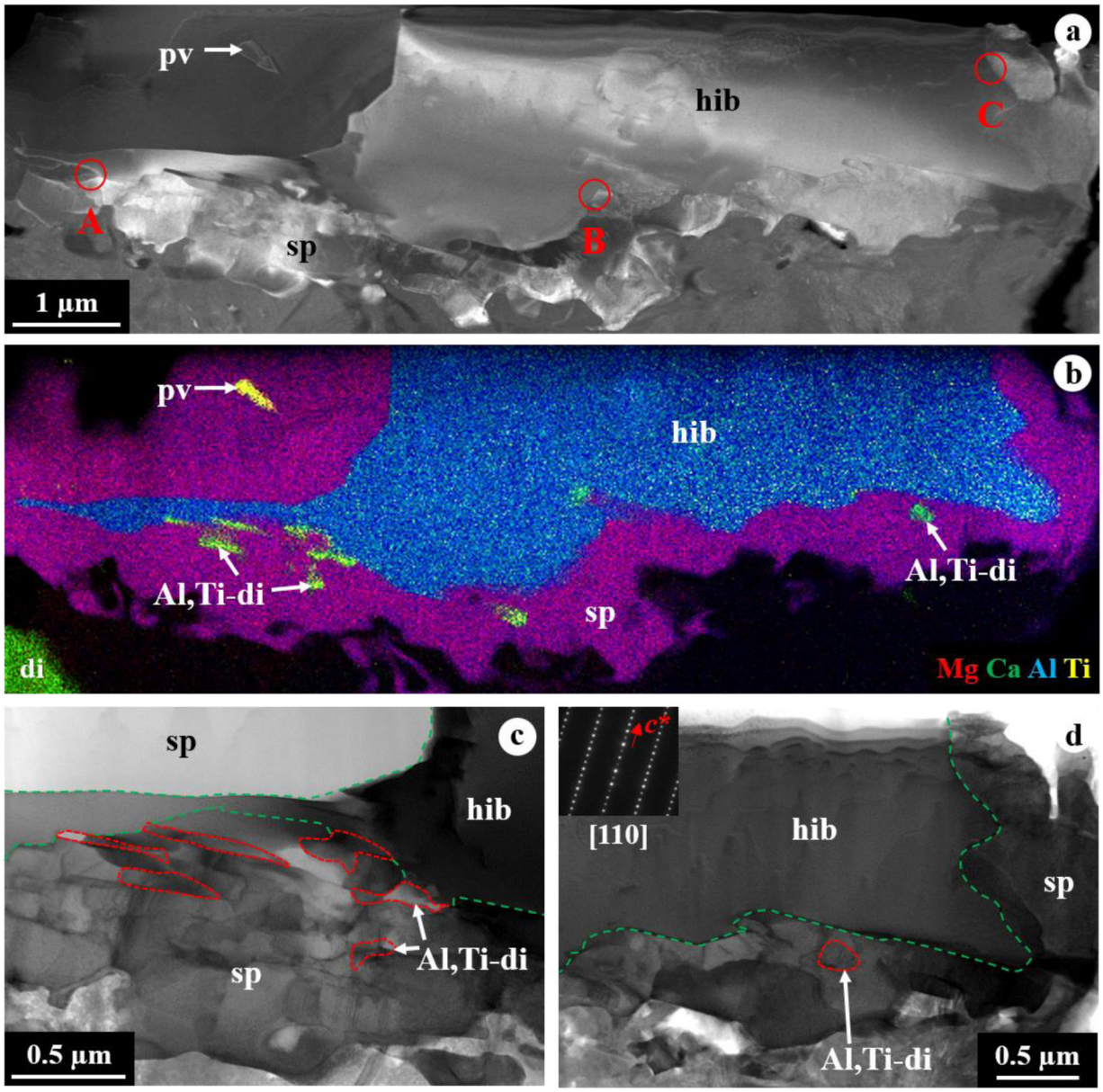

Figure 7.

TEM images of a FIB section from CAI 2–119. (a) DF-STEM image and (b) combined TEM EDX map of the FIB section that consists of a hibonite crystal embedded in spinel with minor Al,Ti-rich diopside and perovskite. In (a), A-C indicate selected areas where diffraction patterns shown in Figure 8 were obtained from the interfaces between hibonite and spinel. (c, d) higher-magnification BF-STEM images of the interfaces of hibonite with spinel and minor Al,Ti-rich diopside. Al,Ti-rich diopside grains are outlined by red dotted lines, whereas the hibonite-spinel grain boundaries are outlined by green dash lines. In (d), inset diffraction patterns are indexed as $[110]_{\text{hibonite}}$. Note that many spinel and Al,Ti-diopside grains appear elongated normal to the *c** axis of hibonite.

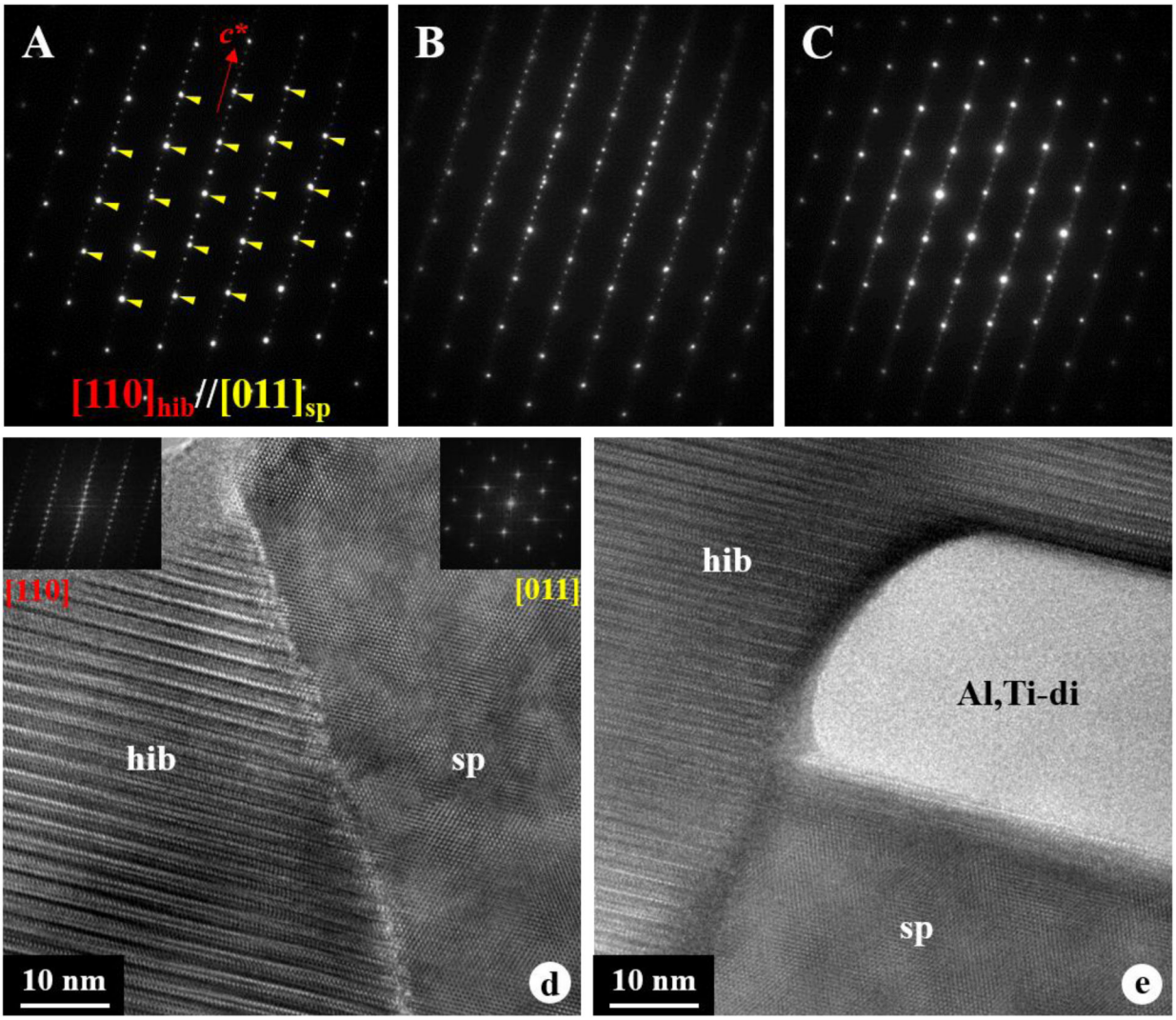

Figure 8.

(a-c) diffraction patterns obtained from three sets of the interfaces between hibonite and adjacent spinel grains in CAI 2–119, showing the same crystallographic orientation relationships between them such that $[110]_{hibonite}//[011]_{spinel}$ and $(001)_{hibonite}//(111)_{spinel}$. Selected areas where the diffraction patterns shown in (a-c) were obtained are indicated in Figure 7. Bright, larger spots indicated by yellow arrows are indexed as the [011] zone axis of spinel, whereas smaller spots are from [110] zone axis of hibonite. (d, e) HR-TEM images obtained from the interfaces of hibonite with adjacent spinel and Al,Ti-rich diopside, showing the crystallographic continuity only between hibonite and spinel. In (d), insets are the FFT patterns indexed as $[110]_{hibonite}$ and $[011]_{spinel}$.

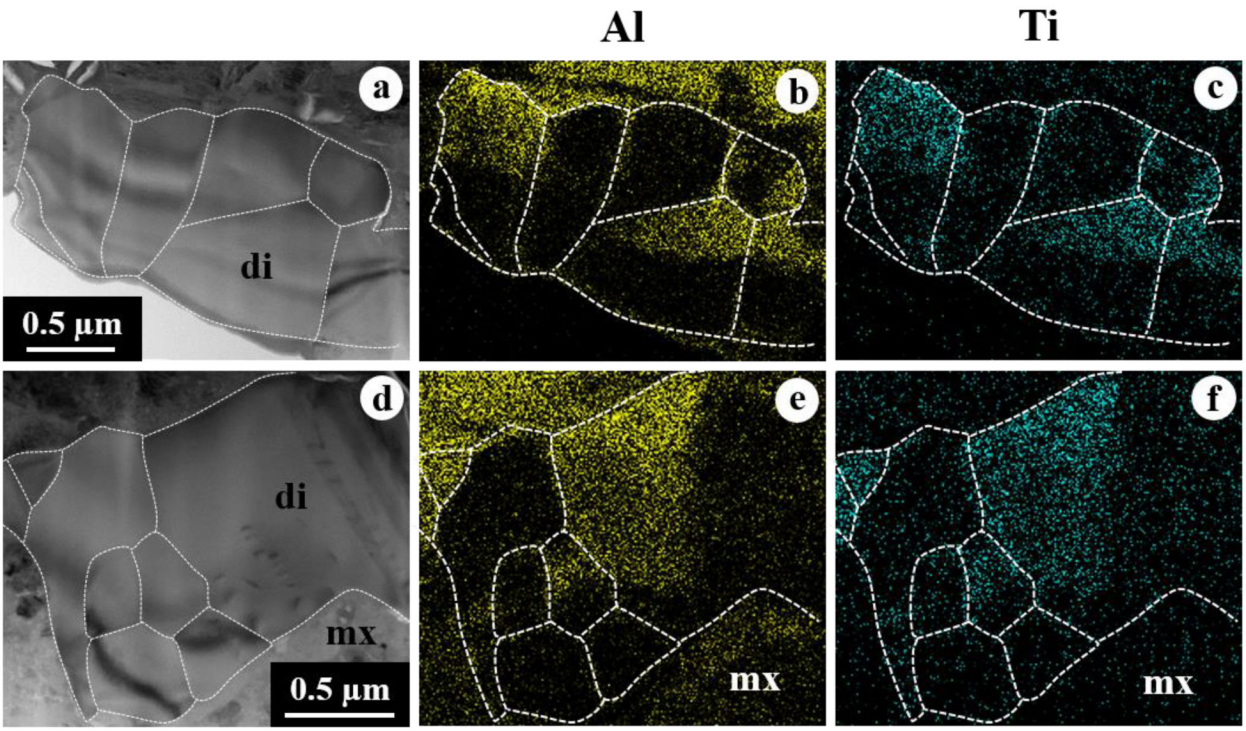

Figure 9.

BF-STEM images (a, d) and corresponding Al and Ti maps (b, c, e, f) obtained using TEM EDX of the diopside rim from CAI 2–119. The Al and Ti contents are heterogeneously distributed within and between diopside grains. The dotted lines represent diopside grain boundaries.

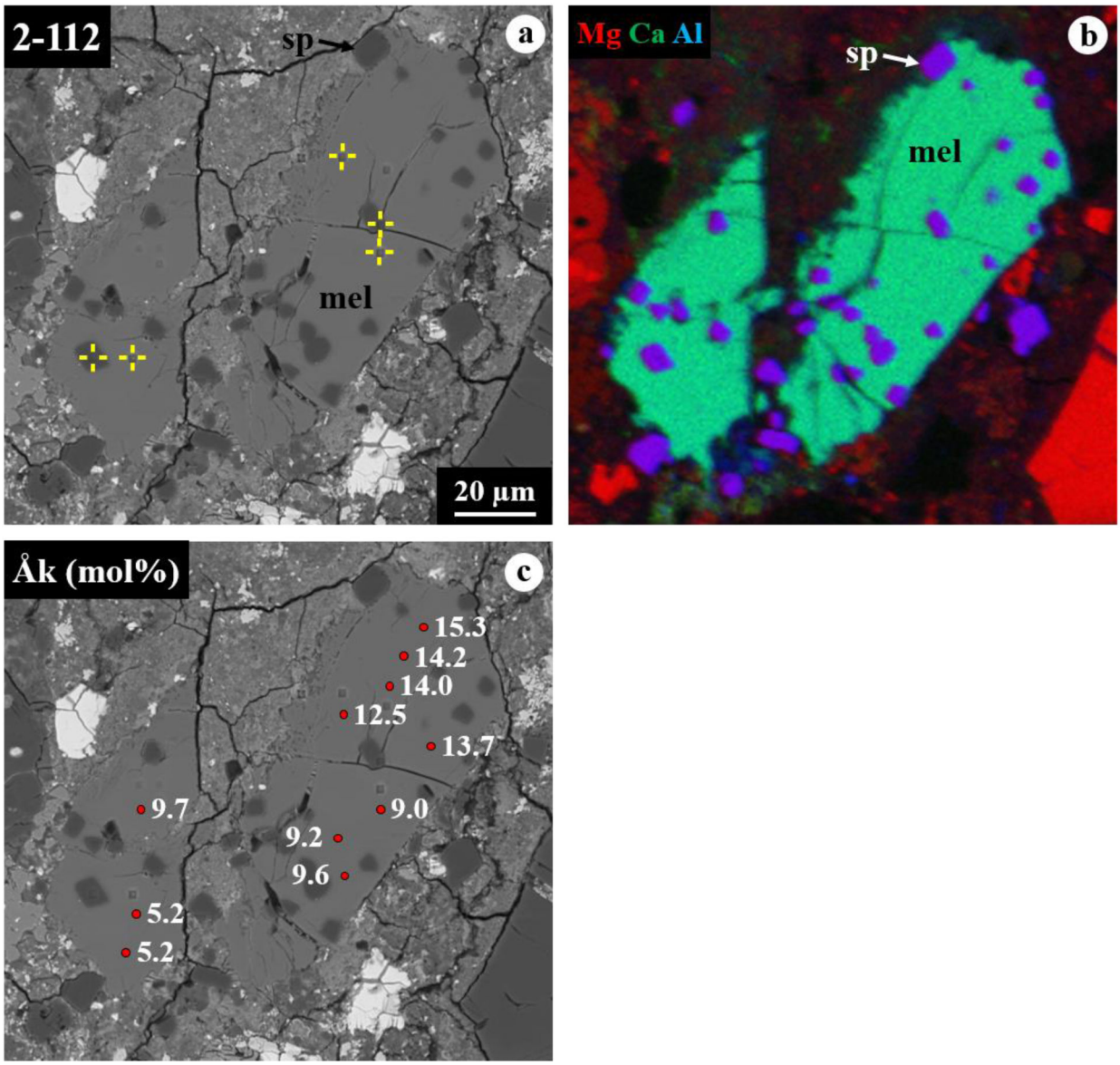

Figure 10.

BSE images (a, c) and combined x-ray map (b) in Mg Kα in red, Ca Kα in green, and Al Kα in blue of melilite-rich CAI 2–112 from ALHA77307. In (c), åkermanite contents are indicated with positions analyzed using electron microprobe. This CAI shows a poikilitic texture with euhedral to subhedral spinel grains enclosed in melilite, in which its åkermanite contents decrease gradually from one end of the crystals to the other. The ims-1290 ion microprobe spot is not appeared here.

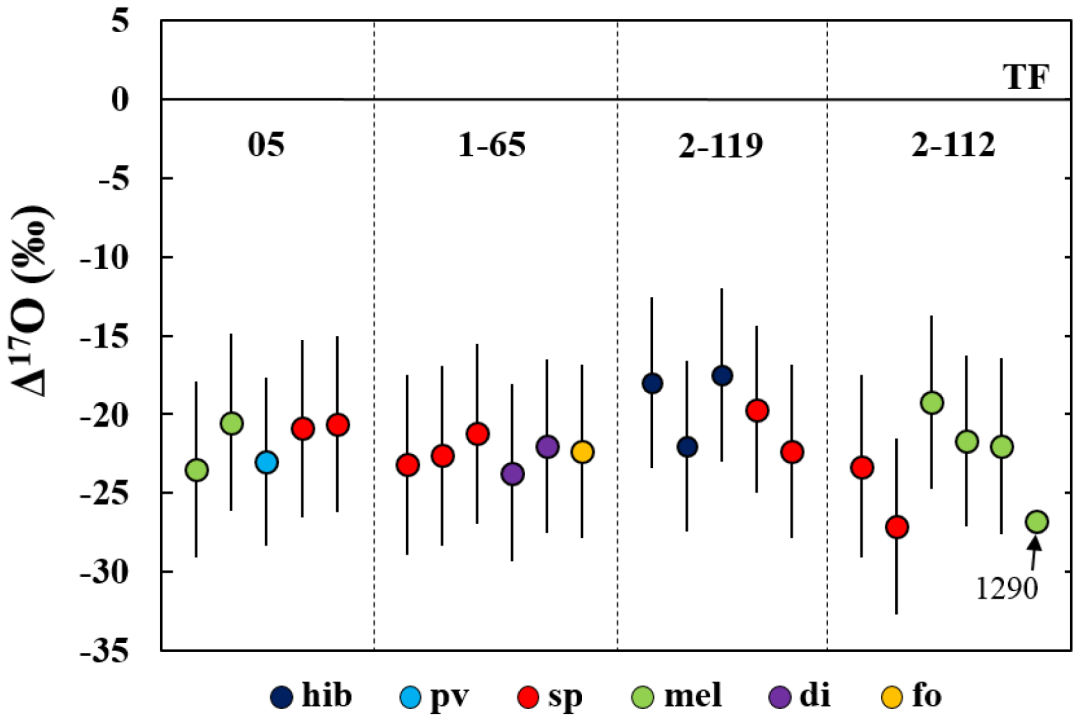

Figure 11.

Oxygen isotopic compositions of individual minerals in four CAIs from ALHA77307. The data are plotted as deviations from the terrestrial fractionation line ($\Delta^{17}O$). All data were measured using NanoSIMS, except for one spot of melilite from CAI 2–112 measured using ims-1290 ion microprobe. The carbonaceous chondrite anhydrous mineral (CCAM) and terrestrial fractionation (TF) lines are shown as reference.

Table 1.

Average compositions (wt%) of individual minerals in four CAIs from ALHA77307 obtained using electron microprobe.

CAI no.	**05**		**1–65**				**2–119**				**2–112**			
mineral	**melilite**		**spinel**		**diopside**		**spinel**		**hibonite**		**spinel**		**melilite**	
No. of analyses	**28**	**1SD**	**9**	**1SD**	**6**	**1SD**	**2**	**1SD**	**5**	**1SD**	**10**	**1SD**	**12**	**1SD**
SiO_2	23.25	0.29	0.11	0.13	51.73	0.91	0.17	0.03	0.18	0.12	0.07	0.01	24.14	0.88
TiO_2	0.02	0.01	0.15	0.05	0.13	0.05	0.13	0.06	2.87	1.09	0.17	0.07	0.08	0.03
Al_2O_3	34.41	0.81	70.83	0.35	5.53	1.27	69.42	0.47	85.77	2.36	70.66	0.46	32.74	1.26
Cr_2O_3	bdl	-	0.08	0.01	0.06	0.03	0.09	0.01	0.02	0.01	0.53	0.17	bdl	-
V_2O_3	bdl	-	0.20	0.03	0.04	0.01	0.20	0.04	0.18	0.10	0.03	0.01	0.02	0.01
FeO	0.25	0.03	0.22	0.06	0.27	0.08	0.78	0.01	0.70	0.04	0.27	0.10	0.25	0.08
MnO	bdl	-	bdl	-	0.02	0.01	0.01	0.01	bdl	-	0.01	0.01	bdl	-
MgO	1.04	0.17	27.58	0.08	17.49	0.49	27.26	0.01	1.93	0.59	27.75	0.19	1.59	0.51
CaO	40.78	0.31	0.10	0.05	24.38	0.34	0.17	0.02	8.37	0.07	0.27	0.07	41.06	0.19
Na_2O	0.01	0.01	bdl	-	0.01	0.01	bdl	-	bdl	-	bdl	-	0.01	0.01
K_2O	0.03	0.01	0.03	0.00	0.03	0.01	0.03	0.01	0.02	0.01	0.02	0.01	0.03	0.01
Total	99.79		99.30		99.69		98.26		100.04		99.78		99.92	
oxygen numbers for the formula	7		4		6		4		19		4		7	
Si	1.065		0.003		1.870		0.004		0.020		0.002		1.105	
Ti	0.001		0.003		0.004		0.002		0.243		0.003		0.003	
Al	1.857		1.995		0.235		1.982		11.364		1.984		1.767	
Cr	-		0.002		0.002		0.002		0.002		0.010		-	
V	-		0.004		0.001		0.004		0.016		0.001		0.001	
Fe	0.009		0.004		0.008		0.016		0.066		0.005		0.010	
Mn	-		-		0.001		-		-		-		-	
Mg	0.071		0.982		0.942		0.984		0.323		0.986		0.108	
Ca	2.001		0.002		0.944		0.004		1.008		0.007		2.014	
Na	0.001		-		0.001		-		-		-		0.001	

CAI no.	**05**		**1–65**				**2–119**				**2–112**			
mineral	**melilite**		**spinel**		**diopside**		**spinel**		**hibonite**		**spinel**		**melilite**	
No. of analyses	**28**	**1SD**	**9**	**1SD**	**6**	**1SD**	**2**	**1SD**	**5**	**1SD**	**10**	**1SD**	**12**	**1SD**
K	0.002		0.001		0.001		0.001		0.003		0.001		0.001	
Total	5.007		2.996		4.009		2.999		13.045		2.999		5.010	
Åk (mol%)[2]	5.4–9.6												5.2–15.3	
ranges of contents (wt%)	MgO: 0.82–1.44				Al_2O_3: 3.81–6.69				TiO_2: 1.35–3.89 MgO: 0.93–2.42				MgO: 0.74–2.23	

[*] bdl: below detection limits.

Table 2.

Oxygen isotopic compositions of individual minerals in four CAIs from ALHA77307.

CAI no.	mineral	$\Delta^{17}O$	2σ
05	melilite	−23.5	5.6
	melilite	−20.5	5.6
	perovskite	−23.0	5.3
	spinel (core)	−20.9	5.6
	spinel (mantle)	−20.6	5.6
	weighted average	−21.7	5.0
1–65	spinel	−23.2	5.7
	spinel	−22.6	5.7
	spinel	−21.2	5.7
	diopside	−23.7	5.6
	diopside	−22.0	5.5
	olivine	−22.3	5.5
	weighted average	−22.5	4.6
2–119	hibonite	−18.0	5.4
	hibonite	−22.0	5.4
	hibonite	−17.5	5.5
	spinel	−19.7	5.3
	spinel	−22.3	5.5
	weighted average	−19.9	4.8
2–112	spinel	−23.3	5.8
	spinel	−27.1	5.6
	melilite	−19.2	5.5
	melilite	−21.7	5.4
	melilite	−22.0	5.6
	weighted average	−22.6	5.0
	melilite (1290)*	−26.8	0.5

* One spot of melilite was measured using the CAMECA ims-1290 ion microprobe at UCLA.